


# Modifications in the angular photoemission time delay in $\text{Ar}@C_{60}^{q=-1}$ : Coulomb confinement resonance as an amplifier of the spin-orbit-interaction-activated interchannel coupling effect

Afsal Thuppilakkadan <sup>1</sup>, Sourav Banerjee <sup>2</sup>, and Hari R. Varma <sup>1,\*</sup>

<sup>1</sup>*School of Physical Sciences, IIT Mandi, Kamand-175075, Himachal Pradesh, India*

<sup>2</sup>*Center for Free-Electron Laser Science CFEL, Deutsches Elektronen-Synchrotron DESY, 22607, Hamburg, Germany*

 (Received 2 August 2022; accepted 28 March 2023; published 10 May 2023)

Coulomb confinement resonances (CCRs) are the main features of the photoionization spectra of an atom inside an anionic fullerene. These CCRs can act as an amplifier to spin-orbit-interaction-activated interchannel coupling (SOIAC) and can lead to discernible signatures of relativistic effects even for low  $Z$  confined atomic systems. The present paper demonstrates this intriguing feature by studying angular photoemission time delay of the  $2p_{3/2}$  subshell of  $\text{Ar}@C_{60}^{-1}$  in the vicinity of the  $2p_{1/2}$  ionization threshold. Here  $2p_{1/2}$  CCR functions as an amplifier to the SOIAC and, thereby, induces significant modifications in the  $2p_{3/2}$  angular time delay through the interchannel coupling. Moreover, the effects of the SOIAC for the spin-up and spin-down photoelectrons are found to be different. All of these suggest that angle-resolved time-delay measurements can reveal the relativistic effects even for the low  $Z$  confined atomic systems, and  $\text{Ar}@C_{60}^{-1}$  is a potential candidate for such experimental scrutiny. The impact of the model parameters on the predicted feature is also critically examined by using different sets of parameters. All of those calculations showed the existence of SOIAC enabled structures in the angular time-delay profile.

DOI: [10.1103/PhysRevA.107.052804](https://doi.org/10.1103/PhysRevA.107.052804)

## I. INTRODUCTION

Recent developments in ultrafast laser technologies have opened up a new route for studying electron dynamics in atoms and molecules. With the help of the state-of-the-art experimental techniques of laser pulses, electron dynamics can now be observed in its natural timescale, i.e., attosecond (as) scale [1–3]. Many theoretical and experimental works have studied the time delay associated with the photoionization of atomic systems [4–13]. The concept of time delay was initially introduced by Wigner [14], Eisenbud [15], and Smith [16] in the realm of the quantum scattering process. The time delay is defined as the energy derivative of the scattering phase shift, which is introduced by the scattering potential. Photoionization can be viewed as the “half-scattering” process; the final state of ionization (photoelectron+ion) is the same as the elastic scattering state of an electron from a residual ion. The connection between the two processes can be obtained by invoking time-reversal symmetry [17]. Using this connection, the idea of time delay can also be extended to photoionization studies.

In photoionization, the time delay follows the same definition of being the energy derivative of the phase, where the phase associated with the complex ionization matrix element is considered. The time delay is an essential measurable parameter along with cross section, angular distribution asymmetric parameter, etc., which provides information about various correlations and dynamics [10,18–26]. Furthermore, the time-delay measurements give direct knowledge of the

phase of the matrix elements, which is otherwise inaccessible. In the pump-probe type measurement techniques, the time delay can be separated into (i) the Wigner contribution and (ii) the Coulomb laser coupling contribution [27]. The first one is the intrinsic delay (also known as the Wigner time delay) due to the single-photon ionization of the target, whereas the latter is due to the interaction of the ejected electron with the combined field of the laser and the residual ion. An interesting feature associated with the time delay is its anisotropy relative to polarization of laser light. It has been theoretically predicted [28,29] and successfully measured experimentally in the recent past [30,31]. In this work, we demonstrate the enhanced anisotropy in the time delay in the region of spin-orbit-interaction-activated interchannel coupling (SOIAC) when an Ar atom is trapped inside a charged fullerene.

The SOIAC is an important relativistic many-body feature which appears in the photoionization spectra of free atoms having high enough  $Z$  [32–36]. It was first observed experimentally for the case of Xe  $3d$  ionization data [33]. The  $3d_{5/2}$  cross section was found to show an extra resonance structure just above the  $3d_{3/2}$  threshold. The origin of this feature is attributed to the presence of a shape resonance in the  $3d_{3/2}$  cross section that appears in this region [32]. This dominant structure in  $3d_{3/2}$  in turn modifies the  $3d_{5/2}$  ionization channels via the interchannel coupling between them, leading to an amenable feature in the  $3d_{5/2}$  cross-section profile. In the absence of shape resonance in  $3d_{3/2}$  such a feature cannot be observed in  $3d_{5/2}$  even if the coupling of spin-orbit split continuum channels is included. In this sense, shape resonances can be considered as an amplifier to the SOIAC. Its discovery and its subsequent successful explanations have

\*Corresponding author: hari@iitmandi.ac.in

prompted a number of research works [33,34,37–42], both theoretical and experimental, in this direction due to its significant impact on the photoionization spectrum even at the qualitative level. The effect of spin-orbit-interaction-activated interchannel coupling (SOIAC) on angular  $3d$  photoemission time delay for free atomic systems has been reported recently [22]. It is unlikely that one would observe any SOIAC effect for free atoms, in general, with smaller atomic number ( $Z$ ) and initial orbital angular momentum quantum number  $l$  less than 2 due to the absence of prominent shape resonances. This is, however, not true when the atom is trapped inside a fullerene cage. Such confined atomic systems provide ways to understand the response of the atom under an external environment and provide impetus to many other fields in physics.

An outstanding feature of the ionization spectra of such confined atomic systems is the presence of confinement oscillations resulting from the interference of an escaping photoelectron and the part of it that gets reflected from the cage. They appear near the thresholds and are present in any subshell irrespective of the value “ $l$ ”. Their existence has been verified experimentally in the recent past [43–46]. The existence of confinement oscillations can facilitate many features that are not common in free atoms. Study of confined atomic systems, therefore, continues to attract significant research attention both from fundamental and applied perspectives [47–52]. These confinement resonances can lead to manifestation of SOIAC in confined systems, similar to the aforementioned role that shape resonances play in high  $Z$  free atomic systems.

The photoionization dynamics of a confined atom becomes more riveting when the surrounding fullerene is charged. The presence of charge on the fullerene shell induces additional huge resonancelike structures near the threshold, known as Coulomb confinement resonances (CCRs), on the ionization spectra of the atom inside. CCRs were predicted initially by Dolmatov and Manson [53] and their genesis was attributed to the modified barrier potential seen by photoelectrons due to the charged nature of the shell. This engenders additional resonance structures in the cross sections, and these CCRs were rigorously examined in a recent work [54]. The presence of CCRs lead to intriguing features in the ionization dynamics [55,56]. These CCRs can mimic the role played by the shape resonances in activating the SOIAC feature in free atoms.

In this work, we show the imprints of CCR enhanced SOIAC in the angular photoemission delay by taking a prototype  $\text{Ar}@C_{60}^{-1}$ , which is a low  $Z$  confined system. Moreover, the results are demonstrated for the photoemission from the  $2p$  subshells, where SOIAC induced features are not even expected for the case of free Ar. What makes it possible in  $\text{Ar}@C_{60}^{-1}$  is the presence of CCR which acts like an amplifier to the SOIAC. The amplification of SOIAC and its consequences on cross section and angular distribution have already been discussed in an earlier work [55]. Here we further show that the enhanced SOIAC results in dramatic angle dependence on the Wigner time delay associated with the electron emission from the  $2p_{3/2}$  subshell of  $\text{Ar}@C_{60}^{-1}$ . The anisotropy in the photoemission time delay emanates due to the presence of CCRs in the  $2p_{1/2}$  ionization channel, which reappears in the  $2p_{3/2}$  ionization channel through interchannel coupling. It

is interesting to note that systems such as  $\text{Ar}@C_{60}^{-1}$  are highly stable [57] and, thus, these systems are potential candidates to explore such relativistic effects in confined atomic systems. It also suggests that the time-delay chronoscopy is very handy to probe the SOIAC features.

A brief review of the theoretical methodologies used in the present work is given in Sec. II. Results and Discussion are given in Sec. III. Finally, in Sec. IV, the Summary and Conclusions are provided. Atomic units are abbreviated as a.u. throughout the manuscript.

## II. THEORY

In an endohedral fullerene, the weak van der Waals force allows the noble gas atom to reside at the geometrical center [58]. This study considers the atom Ar encapsulated at the center of the fullerene  $C_{60}$  anion. A neutral fullerene environment is simulated by a spherically attractive short-range square well potential  $V^{\text{cage}}(r)$ :

$$V^{\text{cage}}(r) = \begin{cases} -U_0, & \text{if } R_{\text{in}} \leq r \leq R_{\text{in}} + \Delta \\ 0, & \text{otherwise} \end{cases}. \quad (1)$$

The cage parameters used in this work are the inner radius  $R_{\text{in}} = 5.8$  a.u., the width  $\Delta = 1.9$  a.u., and the depth  $U_0 = 0.3021$  a.u. This model potential has been used successfully in many theoretical studies [20,59–63]. In the case of a fullerene anion, the potential due to the excess charge is calculated using Gauss’s law and is given by [53,54,56,63,64]

$$V_q(r) = \begin{cases} \frac{q}{R_{\text{in}} + \Delta} & \text{if } 0 < r < R_{\text{in}} + \Delta \\ \frac{q}{r} & \text{otherwise} \end{cases}. \quad (2)$$

Then the effective model potential for a fullerene anion  $C_{60}^q$  is  $V_{cq}(r) = V^{\text{cage}}(r) + V_q(r)$ . This effective potential is added to a free atom’s Dirac-Hartree-Fock (DHF) equation to calculate an endohedral system’s ionization energies and ground-state wave function. We have employed Johnson and Lin’s relativistic random phase approximation (RRPA) formalism [65–67] to study the photoionization dynamics.

The transition amplitude from an initial state  $a$  ( $n, \kappa$ ) to a continuum state  $\bar{a}$  ( $E, \bar{\kappa}$ ) for a linearly polarized photon in the  $\hat{z}$  direction, in electric dipole approximation [20,22,28], is given by

$$T_{10}^{\pm} \equiv [T_{10}^{(1)}]_{v=\pm 1/2} = \sum_{\bar{\kappa}\bar{m}} C_{\bar{l},\bar{m}-v,1/2v}^{\bar{j},\bar{m}} Y_{\bar{l}\bar{m}-v}(\hat{p}) (-1)^{2\bar{j}+j+1-\bar{m}} \times \begin{pmatrix} \bar{j} & 1 & j \\ -\bar{m} & 0 & m \end{pmatrix} D_{1j-\bar{l}\bar{j}}, \quad (3)$$

where the label “ $n$ ” corresponds to the principal quantum number;  $\kappa$  and  $\bar{\kappa}$  are, respectively, the kappa quantum numbers of the initial state and the final state; and the final continuum state has energy  $E$ . In the above equation,

$$D_{1j-\bar{l}\bar{j}} = i^{1-\bar{l}} e^{i\delta_{\bar{\kappa}}} \langle \bar{a} || Q_1^{(1)} || a \rangle \quad (4)$$

is the reduced matrix element, as defined in Ref. [28], with the appropriate phase factor. The photoelectron momentum direction is denoted by  $\hat{p}$  and  $\delta_{\bar{\kappa}}$  is the phase of the final continuum state with  $\bar{\kappa} = \mp(\bar{j} + \frac{1}{2})$  for  $\bar{j} = (\bar{l} \pm \frac{1}{2})$ . Here the labels  $l, j, m$  respectively correspond to the orbital angular momentum, total angular momentum, and magnetic quantum

numbers of the initial state while  $\bar{l}, \bar{j}, \bar{m}$  represent the same but for the final state. In Eq. (3),  $C$  is the Clebsch-Gordan coefficient, and  $Y_{\bar{l}\bar{m}-\nu}(\hat{p})$  is the spherical harmonics.

The electric dipole transition amplitudes for the  $np$  states are given in Ref. [28]. Our interest is to investigate the SOIAC effect in the  $2p_{3/2}$  subshell. The four required angle-resolved transition amplitudes associated with the  $2p_{3/2}$  subshell are listed below:

$$\begin{aligned} [T_{10}^{1+}]_{2p_{3/2}}^{m=\frac{1}{2}} &= \frac{1}{\sqrt{6}} Y_{00} D_{2p_{3/2} \rightarrow \varepsilon s_{1/2}} \\ &\quad - \frac{1}{5\sqrt{6}} Y_{20} D_{2p_{3/2} \rightarrow \varepsilon d_{3/2}} - \frac{1}{5} \sqrt{\frac{3}{2}} Y_{20} D_{2p_{3/2} \rightarrow \varepsilon d_{5/2}}, \end{aligned} \quad (5)$$

$$[T_{10}^{1-}]_{2p_{3/2}}^{m=\frac{1}{2}} = \frac{1}{10} Y_{21} D_{2p_{3/2} \rightarrow \varepsilon d_{3/2}} - \frac{1}{5} Y_{21} D_{2p_{3/2} \rightarrow \varepsilon d_{5/2}}, \quad (6)$$

$$[T_{10}^{1+}]_{2p_{3/2}}^{m=\frac{3}{2}} = -\frac{\sqrt{3}}{10} Y_{21} D_{2p_{3/2} \rightarrow \varepsilon d_{3/2}} - \frac{2\sqrt{3}}{15} Y_{21} D_{2p_{3/2} \rightarrow \varepsilon d_{5/2}}, \quad (7)$$

$$[T_{10}^{1-}]_{2p_{3/2}}^{m=\frac{3}{2}} = \frac{\sqrt{3}}{5} Y_{22} D_{2p_{3/2} \rightarrow \varepsilon d_{3/2}} - \frac{\sqrt{3}}{15} Y_{22} D_{2p_{3/2} \rightarrow \varepsilon d_{5/2}}. \quad (8)$$

Each of these expressions has its own Wigner time delay defined as

$$\tau = \frac{d\eta}{dE}, \quad \text{where } \eta = \tan^{-1} \left[ \frac{\text{Im } T_{10}^{1\pm}}{\text{Re } T_{10}^{1\pm}} \right]. \quad (9)$$

The Wigner time delay averaged over initial  $m$  states and summed over final spins of the photoelectrons is given by the weighted sum for the  $2p_{3/2}$  subshell as

$$\begin{aligned} \mathbb{N} \bar{\tau}_{2p_{3/2}} &= \tau_{2p_{3/2}}^{m=1/2,+} \left| [T_{10}^{1+}]_{2p_{3/2}}^{m=\frac{1}{2}} \right|^2 + \tau_{2p_{3/2}}^{m=1/2,-} \left| [T_{10}^{1-}]_{2p_{3/2}}^{m=\frac{1}{2}} \right|^2 \\ &\quad + \tau_{2p_{3/2}}^{m=3/2,+} \left| [T_{10}^{1+}]_{2p_{3/2}}^{m=\frac{3}{2}} \right|^2 + \tau_{2p_{3/2}}^{m=3/2,-} \left| [T_{10}^{1-}]_{2p_{3/2}}^{m=\frac{3}{2}} \right|^2, \end{aligned} \quad (10)$$

with  $\mathbb{N} = |[T_{10}^{1+}]_{2p_{3/2}}^{m=\frac{1}{2}}|^2 + |[T_{10}^{1-}]_{2p_{3/2}}^{m=\frac{1}{2}}|^2 + |[T_{10}^{1+}]_{2p_{3/2}}^{m=\frac{3}{2}}|^2 + |[T_{10}^{1-}]_{2p_{3/2}}^{m=\frac{3}{2}}|^2$ .

In multichannel RPA formalism, different levels of truncation for the dipole transition channels can be performed to study the SOIAC effect. In the present study, two different levels of calculations are employed. For the first case, all 16 relativistic ionization channels (16ch) originating from the  $1s$ ,  $2s$ ,  $2p$ ,  $3s$ , and  $3p$  subshells are included. Another calculation with fourteen channels (14ch) is executed where the ionization channels from the  $2p_{1/2}$  are excluded. Comparison between these results provides the knowledge about the impact of  $2p_{1/2}$  ionization channels over the channels arising from the  $2p_{3/2}$  subshell. In other words, SOIAC features arising from the coupling between the  $2p_{3/2}$  and  $2p_{1/2}$  channels can be clearly demonstrated by performing 16ch and 14ch calculations.

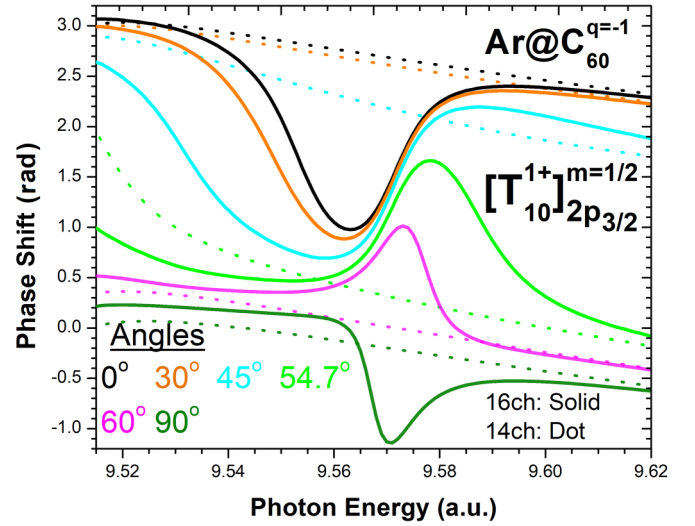


FIG. 1. Phase shift calculated using Eq. (5) for the  $2p_{3/2}$  subshell of  $\text{Ar}@C_{60}^{q=-1}$  with (16ch) and without (14ch)  $2p_{1/2}$  coupling. The upper solid curve (black) corresponds to  $0^\circ$  and the lower solid curve (dark green) corresponds to  $90^\circ$ . All the in-between solid curves starting from the top correspond, in order, to the angles  $30^\circ$ ,  $45^\circ$ ,  $54.7^\circ$ , and  $60^\circ$ , respectively. The same applies to the 14ch curves (dotted curves), which do not show any structures in this region.

### III. RESULTS AND DISCUSSION

The phase shifts associated with  $[T_{10}^{1+}]_{2p_{3/2}}^{m=\frac{1}{2}}$  are calculated for different angles and at two levels of truncation (14ch and 16ch), as mentioned in the previous section, in the region between 9.52 and 9.62 a.u. where SOIAC effects can be observed. Results from these two levels of calculations are shown in Fig. 1 for different angles. For the 14ch case, i.e., without  $2p_{1/2}$  coupling, the phase shift shows a monotonic decrease and the trend is the same for all the angles except for the magic angle. The profiles are clearly angle dependent. The angular anisotropy arises because the transition amplitude, given in Eq. (5), is a combination of two dipole channels ( $2p \rightarrow \varepsilon d$ , and  $2p \rightarrow \varepsilon s$ ) with different angular momentum final states; the associated coefficients have spherical harmonics  $Y_{00}$  and  $Y_{20}$ , among which the former one is the same for all angles, whereas the latter changes its value with different angles. The coupling with  $2p_{1/2}$  channels brings two dramatic changes as depicted in the 16ch curves. The first one is a significant deviation from the monotonic decrease for each angle and the second is a strong enhancement in the angular anisotropy in the vicinity of SOIAC. The dramatic variations in the phase shift are then translated to the time delay because the latter is the energy derivative of the former.

The angular time-delay profiles for 14ch and 16ch associated with  $[T_{10}^{1+}]_{2p_{3/2}}^{m=1/2}$  are shown in Fig. 2. The 16ch time-delay curves show strong angular anisotropy in the SOIAC region. More interestingly, time delay undergoes large excursions, a few thousand of attoseconds, in this region. These features stem from the coupling between the  $2p_{1/2}$  and  $2p_{3/2}$  ionization channels. The presence of  $2p_{1/2}$  CCR strongly enhances the coupling and acts as an amplifier to the SOIAC leading to

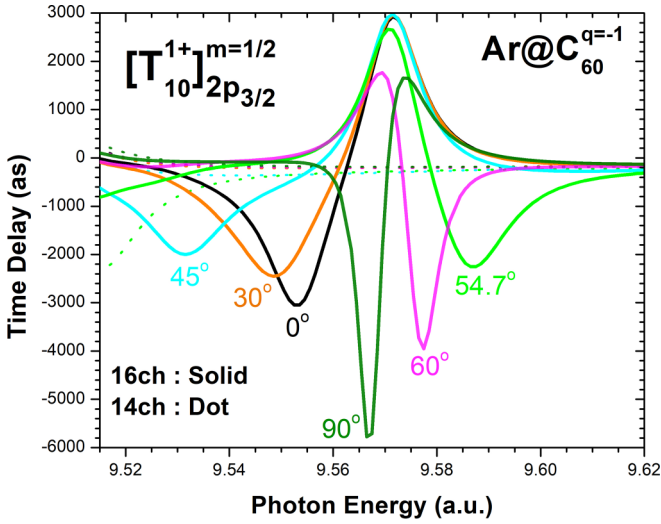


FIG. 2. Angular time delay calculated using Eq. (5) for the  $2p_{3/2}$  subshell of  $\text{Ar@C}_{60}^{-1}$  with (16ch) and without (14ch)  $2p_{1/2}$  coupling. The various angles used in the calculations are indicated near the minimum of each of the solid curves corresponding to each 16ch calculation. The dotted curves correspond to the 14ch calculations and are structureless in the region of interest.

such stupendous deviations in the time-delay profile. It is seen that anisotropy is more in the region below 9.58 a.u. and as the energy increases further the anisotropy is somewhat diminished, except for the magic angle. This can be attributed to the relative importance of each channel in the vicinity of SOIAC. As shown in a previous work [55], in the region before 9.58 a.u., the magnitudes of all possible relativistic channels from  $2p_{3/2}$  have comparable contributions and hence all of them play important roles in the time-delay determination. As a result of the interference among these channels, the time-delay profile in this region shows strong anisotropy. After the photon energy of 9.58 a.u., the  $2p_{3/2} \rightarrow \epsilon d_{5/2}$  matrix element starts to dominate, which leads to the reduction in the anisotropy. In the case of the magic angle ( $54.7^\circ$ ),  $Y_{20}$  is zero, leading the second and the third terms of Eq. (5) to vanish and thereby making the time-delay profile purely due to the  $2p_{3/2} \rightarrow \epsilon s_{1/2}$  matrix element. Hence it behaves differently from the rest. Although  $2p_{3/2} \rightarrow \epsilon s_{1/2}$  is a weak channel, time delay at the magic angle is entirely dictated by this ionization channel. This has an important consequence on the average time delay which will be discussed later in this paper.

It is important to note that the presence of a charge ( $q$ ) on the fullerene is necessary to observe such a feature, which only can induce the CCR [53,54,63,64]. In other words, if the surrounding cage is neutral, the predicted feature will not be present. To illustrate this point, we show in Figs. 3(a) and 3(b), the 16ch results obtained from  $\text{Ar@C}_{60}^{q=0}$  and  $\text{Ar@C}_{60}^{q=-1}$  above their respective  $2p_{1/2}$  thresholds for two different angles. They are plotted against the photoelectron energy since the  $2p_{1/2}$  thresholds differ in both species. The  $2p_{1/2}$  threshold for  $\text{Ar@C}_{60}^{q=0}$  is 9.635 a.u. whereas for  $\text{Ar@C}_{60}^{q=-1}$  it is 9.505 a.u. [55]. Also note the difference in the  $2p_{3/2}$  thresholds; the threshold is at 9.550 a.u. for  $\text{Ar@C}_{60}^{q=0}$ , whereas it is at 9.420 a.u. for  $\text{Ar@C}_{60}^{q=-1}$ . In both cases ( $q = 0$  and  $q = -1$ ),

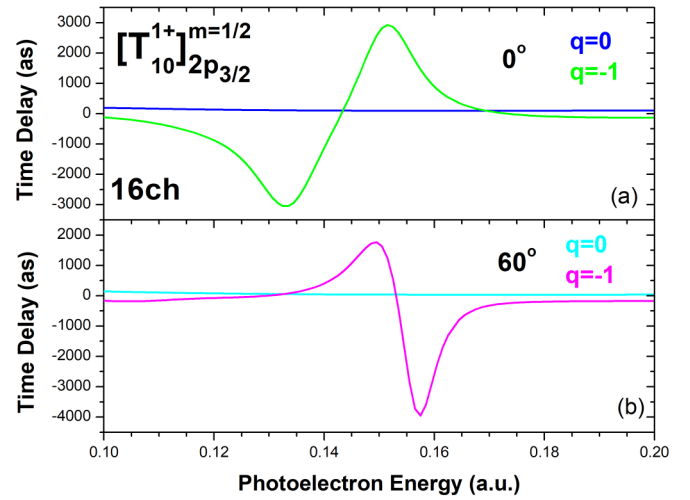


FIG. 3. The upper and lower panels show the 16ch calculations, for  $q = 0$  and  $q = -1$ , corresponding to  $0^\circ$  and  $60^\circ$ , respectively. In both cases  $q = -1$  shows a structure whereas  $q = 0$  is monotonic in the region of interest.

the coupling between the spin-orbit split channels from  $2p_{3/2}$  and  $2p_{1/2}$  is present. However, for the  $q = 0$  case there are no resonance structures irrespective of the presence of coupling. On the other hand, the large CCR structure present in the  $2p_{1/2}$  ionization channels for the case of  $\text{Ar@C}_{60}^{-1}$  makes the coupling between the  $2p_{3/2}$  and  $2p_{1/2}$  ionization channels stronger. This leads to dramatic deviations in the time-delay profiles for both angles in this energy region of interest. The CCR, therefore, can be viewed as an amplifier to the SOIAC effect.

The phase shifts and time delays for  $[T_{10}^{1-}]_{2p_{3/2}}^{m=1/2}$ ,  $[T_{10}^{1+}]_{2p_{3/2}}^{m=3/2}$ , and  $[T_{10}^{1-}]_{2p_{3/2}}^{m=3/2}$  are shown in Figs. 4 and 5, respectively, with 14ch and 16ch channel truncations. The 14ch phase shifts and time delays show a monotonic decrease whereas the 16ch results are dramatically modified due to the CCR amplified SOIAC effect. The phase and time-delay results at both levels of truncation are no more angle dependent. Hence the results are shown only for one particular angle only. The reason for isotropy is that all the terms corresponding to any of the individual amplitudes expressed in Eqs. (6)–(8) contain single spherical harmonics, which gets canceled off while determining the phase. Hence both phase shift and time delay are independent of the angles. Notwithstanding the isotropy in the emission delay, it is interesting to note that the effect of SOIAC appears differently in each of these amplitudes. The time delay associated with  $[T_{10}^{1-}]_{2p_{3/2}}^{m=3/2}$  is only positive whereas it undergoes both positive and negative delays for the other two cases. The spin-up and spin-down electrons associated with  $m = 3/2$  show different sensitivity to energy although they are angular isotropic. On the other hand, the delay associated with  $[T_{10}^{1-}]_{2p_{3/2}}^{m=1/2}$  shows isotropy whereas the corresponding delay for the spin-up electron (i.e., for  $[T_{10}^{1+}]_{2p_{3/2}}^{m=1/2}$ ) is anisotropic (as shown in Fig. 2). The difference in nature of the spin up and spin down in the SOIAC region makes this system an interesting candidate, particularly in the context of spin-resolved time-delay measurements [68–71].

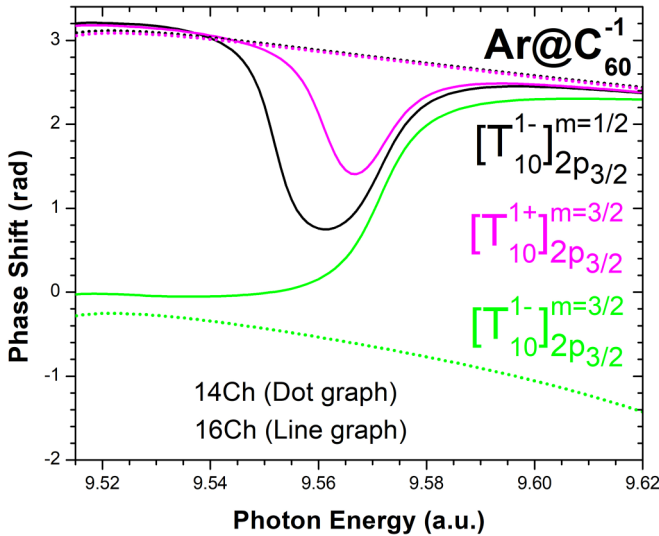


FIG. 4. Phase shift calculated using Eqs. (6)–(8) for the  $2p_{3/2}$  subshell of  $\text{Ar@C}_{60}^{-1}$  with (16ch) and without (14ch)  $2p_{1/2}$  coupling. The solid curves correspond to the 16ch calculations for  $[T_{10}^{1+}]_{2p_{3/2}}^{m=3/2}$  (upper),  $[T_{10}^{1-}]_{2p_{3/2}}^{m=1/2}$  (middle), and  $[T_{10}^{1-}]_{2p_{3/2}}^{m=3/2}$  (lower). The corresponding 14ch results are structureless and are shown with dotted curves in which  $[T_{10}^{1+}]_{2p_{3/2}}^{m=3/2}$ ,  $[T_{10}^{1-}]_{2p_{3/2}}^{m=1/2}$  appear on the top and  $[T_{10}^{1-}]_{2p_{3/2}}^{m=3/2}$  on the bottom part of the figure.

The photoionization time delays from the  $2p_{3/2}$  subshell, i.e., the weighted average over the initial-state magnetic quantum number  $m$ , and summed over the final-state spins of the photoelectrons [from Eq. (10)], are depicted in Fig. 6 for different angles. Both levels of truncation (14ch and 16ch) are shown in the figure. The 14ch time delay shows a monotonic decrease, while the 16ch result is modified due to the SOIAC

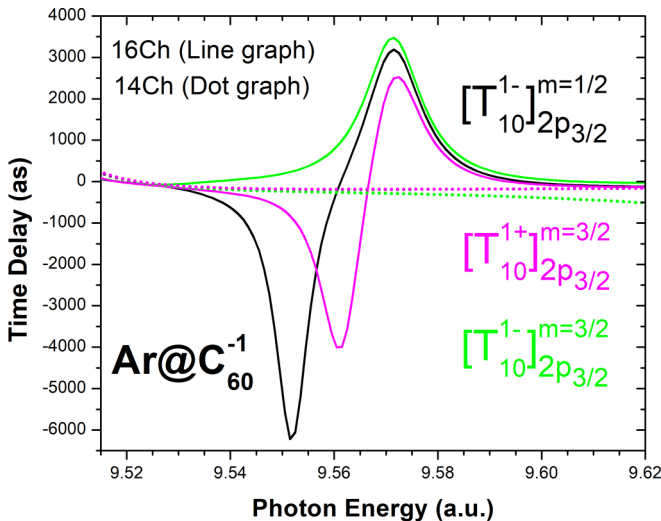


FIG. 5. Angular time delay calculated using eqs. (6)–(8) for the  $2p_{3/2}$  subshell of  $\text{Ar@C}_{60}^{-1}$  with (16ch) and without (14ch)  $2p_{1/2}$  coupling. The solid curves correspond to 16ch calculations and the time delay corresponding to  $[T_{10}^{1-}]_{2p_{3/2}}^{m=3/2}$  have positive values throughout the entire energy region whereas the time delays corresponding to  $[T_{10}^{1-}]_{2p_{3/2}}^{m=1/2}$  and  $[T_{10}^{1+}]_{2p_{3/2}}^{m=3/2}$  show negative and positive values. The dotted curves correspond to the 14ch calculations.

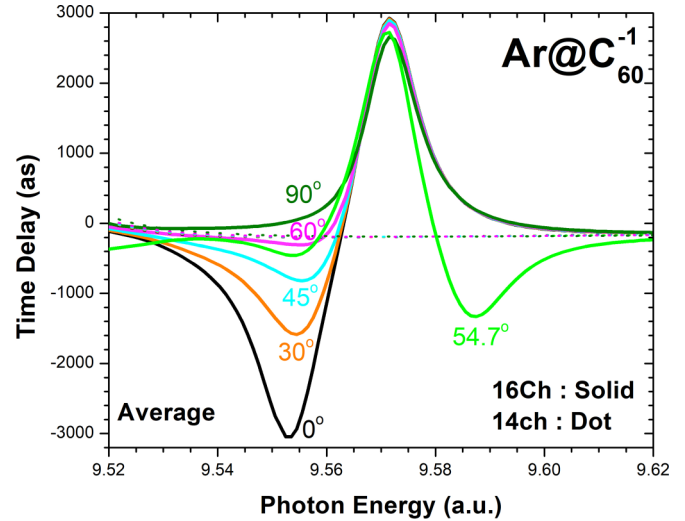


FIG. 6. Weighted average angular time delay calculated using Eq. (10) for the  $2p_{3/2}$  subshell of  $\text{Ar@C}_{60}^{-1}$  with (16ch) and without (14ch)  $2p_{1/2}$  coupling. The various angles used for the calculations are indicated near the minimum of each of the solid curves corresponding to the 16ch calculations. The dotted curves correspond to the 14ch calculations.

effect. The profiles undergo a minimum which is followed by a humplike structure. In the region of the minimum, the average time-delay profile is anisotropic whereas the region above the humplike structure depicts isotropic behavior, except for the magic angle ( $54.7^\circ$ ). This can be directly traced to the features seen in Figs. 2 and 5. The individual time-delay contributions from all transition amplitudes fluctuate significantly below 9.58 a.u., leading to strong angular anisotropy in the region of minimum in Fig. 6. However, above 9.58 a.u., these contributions are relatively small and quantitatively similar, giving rise to the isotropic behavior. The difference in average time delay at the magic angle is directly connected to the feature observed in Fig. 2, where the time delay associated with  $[T_{10}^{1+}]_{2p_{3/2}}^{m=1/2}$  shows a different profile at the magic angle at these energies, which was discussed earlier.

A number of different types of fullerene model potentials are available in the literature [72–77] with different sets of parameters and forms. However, the simple model potentials such as the one employed in the present work continue to be popular because of the ease of calculations and its success in the past predicting important features of endohedral systems. It captures an average effect of the fullerene potential. Even in this simple model different sets of values have been employed for the confinement parameters. In order to check the robustness of the SOIAC induced feature on the angular time delay, the RRPA calculations were repeated systematically for different sets of fullerene parameters. At first calculations were executed by using the values  $R_{\text{in}} = 6.01$  a.u.,  $\Delta = 1.25$  a.u., and  $U_0 = 0.422$  a.u. [73] [set (i)]. Previous studies using this set of values have shown better agreement with experimental results on photoionization cross section [46]. Further, the calculations were repeated by using another set of values [set(ii)]  $R_{\text{in}} = 5.262$  a.u.,  $\Delta = 2.91$  a.u., and  $U_0 = 0.2599$  a.u., which had been successfully employed

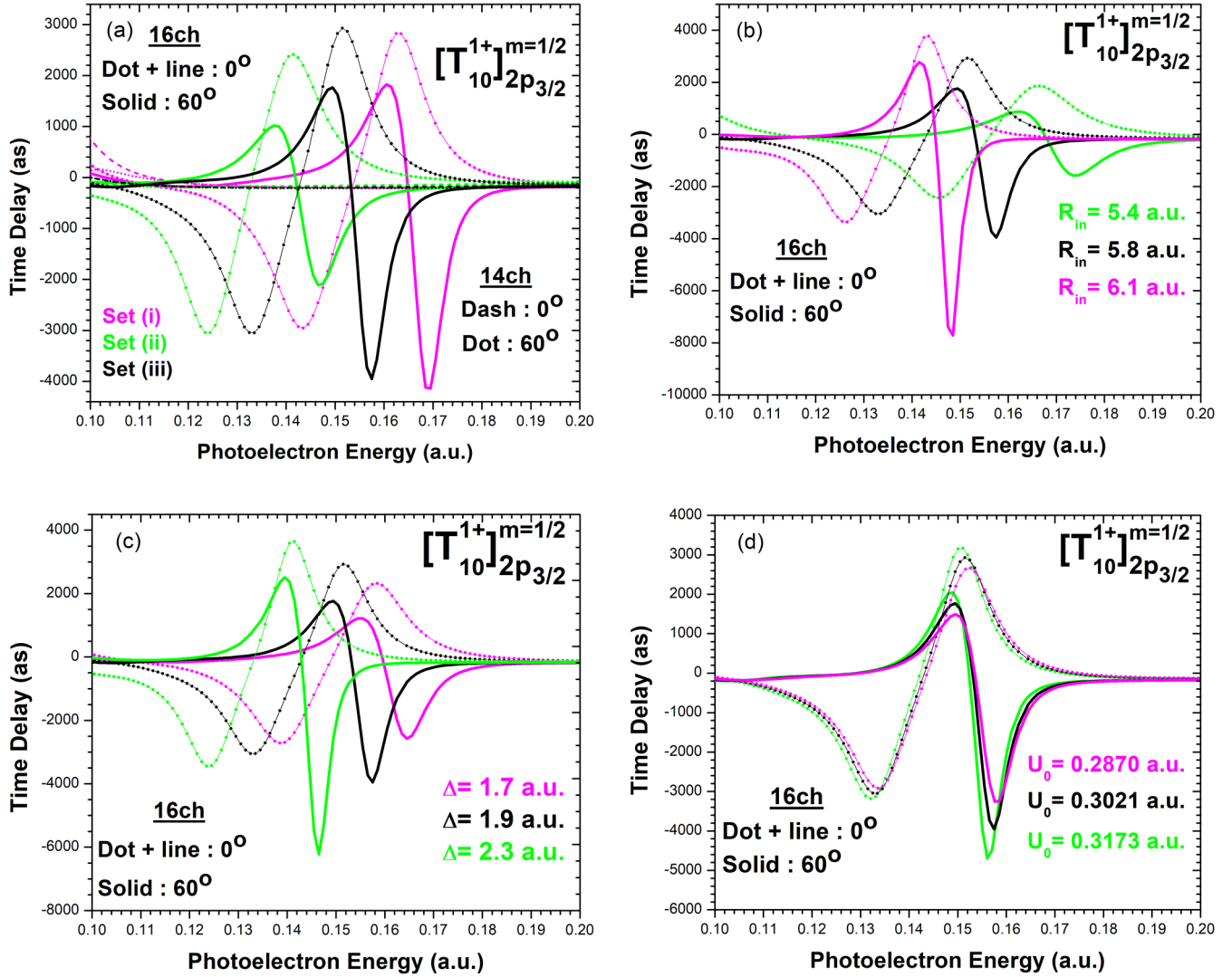


FIG. 7. Angular time delay calculated using Eq. (5) in the manuscript (a) using parameters listed in set (i), set (ii), and set (iii), and afterwards, using set (iii) parameters but varying only (b) the radius, (c) the width, and (d) the depth of the potential. In (a) both 14ch and 16ch results are shown for the angles  $0^\circ$  and  $60^\circ$  whereas in (b–d) only 16ch results are presented for both angles.

in scattering studies of fullerene [77]. The results obtained from these modified parameters along with the original parameters used in the present work ( $R_{in} = 5.8$  a.u.,  $\Delta = 1.9$  a.u., and  $U_0 = 0.3021$  a.u. ([set(iii)]) are displayed in Fig. 7(a) for two different angles  $0^\circ$  and  $60^\circ$  (both 14ch and 16ch). The 14ch calculations do not show any structures in the SOIAC region, whereas the spin-orbit-activated structures arising due to  $2p_{1/2}$  coupling are present in all 16ch calculations for sets (i–iii). As can be seen, the SOIAC induced time delay is qualitatively the same in all model potential calculations, despite its quantitative differences. It clearly demonstrates that the existence of such SOIAC effect is irrefutable in the angular time-delay profile although its quantitative features are susceptible to various model potentials. The SOIAC region is far away from the region of plasmon resonances in  $C_{60}$  [78] which implies that even in more complex molecular-level calculations, the predicted effect in the time delay cannot be eliminated, while the quantitative details are likely to alter.

The nature of variations in the above-mentioned three sets makes it impossible to do any systematic analysis. Therefore, an additional study has been carried out utilizing set (iii), but changing one parameter at a time in a systematic manner, i.e., by changing either the  $R_{in}$ ,  $\Delta$ , or the  $U_0$  of the potential while retaining the other parameter values the same. The results obtained are shown in Figs. 7(b)–7(d). Regardless of the settings of the parameters used, it can be observed that SOIAC enabled structure is present in all of these calculations even though their quantitative details vary. For the sake of brevity the 14ch results are not depicted as they do not show any structure due to the absence of the coupling between the relativistic split channels.

It should be noted that the SOIAC effect was strengthened in the  $2p_{3/2}$  photoionization time delay by the presence of Coulomb confinement resonance (CCR) in the  $2p_{1/2}$  ionization channel. As discussed in earlier papers [53–56,63], the charged character of the fullerene accounts for the CCRs and these resonance structures depend on the barrier height

seen by the escaping photoelectron. Using these, the nature of sensitivity of the SOIAIC effect in the time-delay profile can be easily understood. Therefore, it is anticipated that the change in fullerene potential will impact the CCRs and in turn modify the SOIAIC induced feature.

Figures 7(b)–7(d) depict the  $2p_{3/2}$  time delay related to  $[T_{10}^{1+}]_{2p_{3/2}}^{m=1/2}$  for various fullerene parameters with 16ch calculations. These figures depict a time delay at  $0^\circ$  and  $60^\circ$  to illustrate how these computations are angularly dependent. In all these cases, the time delay shows a prominent SOIAIC effect. In every case, it has been observed that the resonance structure is shifting to the lower energy region. This is because the resonance condition shifts to lower energy as the barrier height is lowered. The variations in the barrier height with regard to the parameters of the confining potential were shown in the earlier paper [54]. The positions of the resonance structure in the time-delay profile somewhat remain the same in Fig. 7(d). This can also be understood from the fact that, in this case, only the confinement well depth is varied but the barrier height remains the same. These findings show that time delay is sensitive to the fullerene model parameters and, however, that the SOIAIC effect is guaranteed in all the cases.

#### IV. SUMMARY AND CONCLUSIONS

The effect of spin-orbit-interaction-activated interchannel coupling (SOIAIC) on the Wigner angular time delay in the photoionization channels from the  $2p_{3/2}$  subshell has been studied for  $\text{Ar}@C_{60}^{-1}$ . The calculations are performed at two different levels of truncation in order to elucidate the effect of the spin-orbit interchannel coupling effect for such a low  $Z$  confined atomic system. The presence of CCR in  $2p_{1/2}$  ionization channels strengthens the coupling and thus acts like an amplifier to the SOIAIC. The enhanced SOIAIC induces dramatic features in the phase shift and time-delay profiles. Strong angular and energy dependences are found for the photoemission of a spin-up photoelectron associated with the angle-resolved transition amplitude  $[T_{10}^{1+}]^{m=1/2}$ . On the other hand, the corresponding spin-down electron has only energy

dependence and shows angular isotropy. Similarly, time delays associated with  $[T_{10}^{+}]^{m=3/2}$  and  $[T_{10}^{-}]^{m=3/2}$  show different SOIAIC features although they show angular isotropy. The difference in nature of spin-up and spin-down electrons in the SOIAIC region makes this system a potential candidate for spin-resolved time-delay measurements [79] since  $\text{Ar}@C_{60}^{-1}$  is a highly stable configuration. The impact of the model parameters on the predicted enhancement is also tested by changing the values of these parameters. In all the different sets of model parameters, the predicted features are found to be present and are in agreement at least qualitatively, which shows the robustness of the current results. However, the model potential considered here includes only the average effects of the anionic fullerene environment. A sophisticated calculation that explicitly includes the electronic structure present in  $C_{60}^{-1}$  would have more features coming from, for example, the additional bound states present in the system [80]. Nevertheless, the present work predicts the unusual features induced by the anionic fullerene on the angular time-delay spectrum of the atom inside, and we hope this would stimulate more sophisticated calculations in this direction.

The spin-averaged time-delay profiles are anisotropic in the region where all the possible dipole ionization channels compete among each other, whereas it follows isotropic behavior when the  $2p_{3/2} \rightarrow \epsilon d_{5/2}$  transition channel starts dominating. The excursions of the time delay in all the cases are found to be large ( $\sim$  a few thousands of attoseconds) in the SOAIC region and also fluctuate between positive and negative values. All these features qualify this endohedral anionic system as a possible candidate for probing the SOIAIC effect in low  $Z$  confined atomic systems. Although we showed results only for the case of  $\text{Ar}@C_{60}^{-1}$ , such dramatic modifications can be observed in other systems as well where CCR amplified SOIAIC exists.

#### ACKNOWLEDGMENT

H.R.V. appreciates the funding received from DST-SERB (India) under Grants No. EMR/2016/002695 and No. CRG/2022/002309.

- 
- [1] A. N. Pfeiffer, C. Cirelli, M. Smolarski, D. Dimitrovski, M. Abu-samaha, L. B. Madsen, and U. Keller, Attoclock reveals natural coordinates of the laser-induced tunnelling current flow in atoms, *Nat. Phys.* **8**, 76 (2012).
  - [2] H. G. Muller, Reconstruction of attosecond harmonic beating by interference of two-photon transitions, *Appl. Phys. B* **74**, s17 (2002).
  - [3] J. Itatani, F. Quéré, G. L. Yudin, M. Y. Ivanov, F. Krausz, and P. B. Corkum, Attosecond Streak Camera, *Phys. Rev. Lett.* **88**, 173903 (2002).
  - [4] S. Zhong, J. Vinbladh, D. Busto, R. J. Squibb, M. Isinger, L. Neoričić, H. Laurell, R. Weissenbilder, C. L. Arnold, R. Feifel, J. M. Dahlström, G. Wendin, M. Gisselbrecht, E. Lindroth, and A. L'Huillier, Attosecond electron–spin dynamics in Xe  $4d$  photoionization, *Nat. Commun.* **11**, 5042 (2020).
  - [5] X. Yu, M. Han, Z. Guo, and Y. Liu, Intrinsic resonant photoionization time delay of hydrogen atoms probed with attosecond beating of asymmetrical photon transitions, *Phys. Rev. A* **104**, 063108 (2021).
  - [6] M. Sabbar, S. Heuser, R. Boge, M. Lucchini, T. Carette, E. Lindroth, L. Gallmann, C. Cirelli, and U. Keller, Resonance Effects in Photoemission Time Delays, *Phys. Rev. Lett.* **115**, 133001 (2015).
  - [7] S. Kosugi, F. Koike, M. Iizawa, M. Oura, T. Gejo, K. Tamasaku, J. R. Harries, R. Guillemin, M. N. Piancastelli, M. Simon, and Y. Azuma, Fluorescence Time Delay in Multistep Auger Decay As an Internal Clock, *Phys. Rev. Lett.* **124**, 183001 (2020).
  - [8] K. Klünder, J. M. Dahlström, M. Gisselbrecht, T. Fordell, M. Swoboda, D. Guénot, P. Johnsson, J. Caillat, J. Mauritsson, A. Maquet, R. Taïeb, and A. L'Huillier, Probing Single-Photon Ionization on the Attosecond Time Scale, *Phys. Rev. Lett.* **106**, 143002 (2011).
  - [9] A. S. Kheifets, S. Saha, P. C. Deshmukh, D. A. Keating, and S. T. Manson, Dipole phase and photoelectron group

- delay in inner-shell photoionization, *Phys. Rev. A* **92**, 063422 (2015).
- [10] D. A. Keating, S. T. Manson, V. K. Dolmatov, A. Mandal, P. C. Deshmukh, F. Naseem, and A. S. Kheifets, Intershell-correlation-induced time delay in atomic photoionization, *Phys. Rev. A* **98**, 013420 (2018).
- [11] M. Isinger, R. J. Squibb, D. Busto, S. Zhong, A. Harth, D. Kroon, S. Nandi, C. L. Arnold, M. Miranda, J. M. Dahlström, E. Lindroth, R. Feifel, M. Gisselbrecht, and A. L'Huillier, Photoionization in the time and frequency domain, *Science* **358**, 893 (2017).
- [12] P. Hockett, E. Frumker, D. M. Villeneuve, and P. B. Corkum, Time delay in molecular photoionization, *J. Phys. B: At., Mol. Opt. Phys.* **49**, 095602 (2016).
- [13] T. Barillot, C. Cauchy, P.-A. Hervieux, M. Gisselbrecht, S. E. Canton, P. Johnsson, J. Laksman, E. P. Mansson, J. M. Dahlström, M. Magrakvelidze, G. Dixit, M. E. Madjet, H. S. Chakraborty, E. Suraud, P. M. Dinh, P. Wopperer, K. Hansen, V. Lorient, C. Bordas, S. Sorensen *et al.*, Angular asymmetry and attosecond time delay from the giant plasmon resonance in  $C_{60}$  photoionization, *Phys. Rev. A* **91**, 033413 (2015).
- [14] E. P. Wigner, Lower limit for the energy derivative of the scattering phase shift, *Phys. Rev.* **98**, 145 (1955).
- [15] L. Eisenbud, The formal properties of nuclear collisions, Ph.D. thesis, Princeton University, 1948.
- [16] F. T. Smith, Lifetime matrix in collision theory, *Phys. Rev.* **118**, 349 (1960).
- [17] P. C. Deshmukh and S. Banerjee, Time delay in atomic and molecular collisions and photoionisation/photodetachment, *Int. Rev. Phys. Chem.* **40**, 127 (2021).
- [18] S. Saha, J. Jose, P. C. Deshmukh, G. Aravind, V. K. Dolmatov, A. S. Kheifets, and S. T. Manson, Wigner time delay in photodetachment, *Phys. Rev. A* **99**, 043407 (2019).
- [19] S. Saha, P. C. Deshmukh, A. S. Kheifets, and S. T. Manson, Dominance of correlation and relativistic effects on photodetachment time delay well above threshold, *Phys. Rev. A* **99**, 063413 (2019).
- [20] A. Mandal, P. C. Deshmukh, A. S. Kheifets, V. K. Dolmatov, and S. T. Manson, Angle-resolved Wigner time delay in atomic photoionization: The  $4d$  subshell of free and confined Xe, *Phys. Rev. A* **96**, 053407 (2017).
- [21] A. Ganesan, S. Banerjee, P. C. Deshmukh, and S. T. Manson, Photoionization of Xe  $5s$ : Angular distribution and Wigner time delay in the vicinity of the second Cooper minimum, *J. Phys. B: At., Mol. Opt. Phys.* **53**, 225206 (2020).
- [22] S. Banerjee, P. C. Deshmukh, A. S. Kheifets, and S. T. Manson, Effects of spin-orbit-interaction-activated interchannel coupling on photoemission time delay, *Phys. Rev. A* **101**, 043411 (2020).
- [23] S. Banerjee, P. C. Deshmukh, V. K. Dolmatov, S. T. Manson, and A. S. Kheifets, Strong dependence of photoionization time delay on energy and angle in the neighborhood of Fano resonances, *Phys. Rev. A* **99**, 013416 (2019).
- [24] S. Saha, A. Mandal, J. Jose, H. R. Varma, P. C. Deshmukh, A. S. Kheifets, V. K. Dolmatov, and S. T. Manson, Relativistic effects in photoionization time delay near the Cooper minimum of noble-gas atoms, *Phys. Rev. A* **90**, 053406 (2014).
- [25] M. Kotur, D. Guénot, Á. Jiménez-Galán, D. Kroon, E. W. Larsen, M. Louisy, S. Bengtsson, M. Miranda, J. Mauritsson, C. L. Arnold, S. E. Canton, M. Gisselbrecht, T. Carette, J. M. Dahlström, E. Lindroth, A. Maquet, L. Argenti, F. Martín, and A. L'Huillier, Spectral phase measurement of a Fano resonance using tunable attosecond pulses, *Nat. Commun.* **7**, 10566 (2016).
- [26] V. Gruson, L. Barreau, Á. Jiménez-Galán, F. Risoud, J. Caillat, A. Maquet, B. Carré, F. Lepetit, J.-F. Hergott, T. Ruchon, L. Argenti, R. Taïeb, F. Martín, and P. Salières, Attosecond dynamics through a Fano resonance: Monitoring the birth of a photoelectron, *Science* **354**, 734 (2016).
- [27] R. Pazourek, S. Nagele, and J. Burgdörfer, Time-resolved photoemission on the attosecond scale: Opportunities and challenges, *Farad. Discuss.* **163**, 353 (2013).
- [28] A. Kheifets, A. Mandal, P. C. Deshmukh, V. K. Dolmatov, D. A. Keating, and S. T. Manson, Relativistic calculations of angle-dependent photoemission time delay, *Phys. Rev. A* **94**, 013423 (2016).
- [29] I. A. Ivanov and A. S. Kheifets, Angle-dependent time delay in two-color XUV+IR photoemission of He and Ne, *Phys. Rev. A* **96**, 013408 (2017).
- [30] C. Cirelli, C. Marante, S. Heuser, C. L. M. Petersson, Á. J. Galán, L. Argenti, S. Zhong, D. Busto, M. Isinger, S. Nandi, S. Maclot, L. Rading, P. Johnsson, M. Gisselbrecht, M. Lucchini, L. Gallmann, J. M. Dahlström, E. Lindroth, A. L'Huillier, F. Martín *et al.*, Anisotropic photoemission time delays close to a Fano resonance, *Nat. Commun.* **9**, 955 (2018).
- [31] S. Heuser, Á. J. Galán, C. Cirelli, C. Marante, M. Sabbar, R. Boge, M. Lucchini, L. Gallmann, I. Ivanov, A. S. Kheifets, J. M. Dahlström, E. Lindroth, L. Argenti, F. Martín, and U. Keller, Angular dependence of photoemission time delay in helium, *Phys. Rev. A* **94**, 063409 (2016).
- [32] M. Y. Amusia, L. V. Chernysheva, S. T. Manson, A. M. Msezane, and V. Radojević, Strong Electron Correlation in Photoionization of Spin-Orbit Doublets, *Phys. Rev. Lett.* **88**, 093002 (2002).
- [33] A. Kivimäki, U. Hergenhahn, B. Kempgens, R. Hentges, M. N. Piancastelli, K. Maier, A. Rüdél, J. J. Tulkki, and A. M. Bradshaw, Near-threshold study of Xe  $3d$  photoionization, *Phys. Rev. A* **63**, 012716 (2000).
- [34] T. Richter, E. Heinecke, P. Zimmermann, K. Godehusen, M. Yalçinkaya, D. Cubaynes, and M. Meyer, Outstanding Spin-Orbit-Activated Interchannel Coupling in the Cs and Ba  $3d$  Photoemission, *Phys. Rev. Lett.* **98**, 143002 (2007).
- [35] M. Y. Amusia, A. S. Baltenkov, L. V. Chernysheva, Z. Felfli, S. T. Manson, and A. Z. Msezane, Effects of spin-orbit activated interchannel coupling on dipole photoelectron angular distribution asymmetry parameters, *J. Phys. B: At., Mol. Opt. Phys.* **37**, 937 (2004).
- [36] J. Jose, S. Baral, P. C. Deshmukh, and S. T. Manson, Relativistic and correlation effects in the photoionization dynamics of oganesson ( $Z = 118$ ): Spin-orbit-interaction-activated interchannel coupling effects, *Phys. Rev. A* **102**, 022813 (2020).
- [37] S. Minemoto, T. Teramoto, T. Majima, T. Mizuno, J. H. Mun, S. H. Park, S. Kwon, A. Yagishita, and D. Toffoli, Photoelectron angular distribution studies for two spin-orbit-split components of Xe  $3d$  subshell: A critical comparison between theory and experiment, *J. Phys. B: At., Mol. Opt. Phys.* **54**, 105003 (2021).
- [38] M. Y. Amusia, A. S. Baltenkov, L. V. Chernysheva, Z. Felfli, S. T. Manson, and A. Z. Msezane, Correlation structure



- in nondipole photoionization, *Phys. Rev. A* **67**, 060702(R) (2003).
- [39] H. Farrokhpour, M. Alagia, M. Y. Amusia, L. Avaldi, L. V. Chernysheva, M. Coreno, M. De Simone, R. Richter, S. Stranges, and M. Tabrizchi, Observation of the spin-orbit activated interchannel coupling in the  $3d$  photoionization of caesium atoms, *J. Phys. B: At., Mol. Opt. Phys.* **39**, 765 (2006).
- [40] H. Farrokhpour, M. Alagia, L. Avaldi, M. Bamdad, M. Coreno, P. Decleva, M. De Simone, R. Richter, S. Stranges, M. Tabrizchi, and D. Toffoli, Spin-orbit-activated interchannel coupling in the  $3d$  photoionization of barium atoms, *J. Phys. B: At., Mol. Opt. Phys.* **40**, 4005 (2007).
- [41] S. S. Kumar, T. Banerjee, P. C. Deshmukh, and S. T. Manson, Spin-orbit-interaction activated interchannel coupling in dipole and quadrupole photoionization, *Phys. Rev. A* **79**, 043401 (2009).
- [42] V. Radojević, D. M. Davidović, and M. Y. Amusia, Near-threshold photoionization of the Xe  $3d$  spin-orbit doublet: Relativistic, relaxation, and intershell interaction effects, *Phys. Rev. A* **67**, 022719 (2003).
- [43] R. A. Phaneuf, A. L. D. Kilcoyne, N. B. Aryal, K. K. Baral, D. A. Esteves-Macaluso, C. M. Thomas, J. Hellhund, R. Lomsadze, T. W. Gorczyca, C. P. Balance *et al.*, Probing confinement resonances by photoionizing Xe inside a  $C_{60}^+$  molecular cage, *Phys. Rev. A* **88**, 053402 (2013).
- [44] A. Müller, S. Schippers, M. Habibi, D. Esteves, J. C. Wang, R. A. Phaneuf, A. L. D. Kilcoyne, A. Aguilar, and L. Dunsch, Significant Redistribution of Ce  $4d$  Oscillator Strength Observed in Photoionization of Endohedral Ce@C $82^+$  Ions, *Phys. Rev. Lett.* **101**, 133001 (2008).
- [45] A. Muller, D. Kilcoyne, S. Schippers, and R. A. Phaneuf, Experimental studies on photoabsorption by endohedral fullerene ions with a focus on Xe@C $60^+$  confinement resonances, *Phys. Scr.* **96**, 064004 (2021).
- [46] A. L. D. Kilcoyne, A. Aguilar, A. Müller, S. Schippers, C. Cisneros, G. Alna'Washi, N. B. Aryal, K. K. Baral, D. A. Esteves, C. M. Thomas, and R. A. Phaneuf, Confinement Resonances in Photoionization of Xe@C $60^+$ , *Phys. Rev. Lett.* **105**, 213001 (2010).
- [47] H. Nie, C. Zhao, Z. Shi, C. Jia, and X. Guo, Single-molecule fullerenes: Current stage and perspective, *ACS Mater. Lett.* **4**, 1037 (2022).
- [48] J. Meng, D. Wang, P. C. Wang, L. Jia, C. Chen, and X.-J. Liang, Biomedical activities of endohedral metallofullerene optimized for nanopharmaceutics, *J. Nanosci. Nanotechnol.* **10**, 8610 (2010).
- [49] W. Harneit, *Spin Quantum Computing with Endohedral Fullerenes in Endohedral Fullerenes: Electron Transfer and Spin* (Springer, Cham, Switzerland, 2017), pp. 297–324.
- [50] R. T. Harding, S. Zhou, J. Zhou, T. Lindvall, W. K. Myers, A. Ardavan, G. A. D. Briggs, K. Porfyrakis, and E. A. Laird, Spin Resonance Clock Transition of the Endohedral Fullerene  $^{15}\text{N}@C_{60}$ , *Phys. Rev. Lett.* **119**, 140801 (2017).
- [51] J. Grebowski and G. Litwinienko, Metallofullerenols in biomedical applications, *Eur. J. Med. Chem.* **238**, 114481 (2022).
- [52] B. X. Vuong, N. Hajali, A. Asadi, A. A. Baqer, S. K. Hachim, and G. Canli, Drug delivery assessment of an iron-doped fullerene cage towards thiotepa anticancer drug, *Inorg. Chem. Commun.* **141**, 109558 (2022).
- [53] V. K. Dolmatov and S. T. Manson, Photoionization of atoms encapsulated in endohedral ions  $A@C_{60}^{\pm z}$ , *Phys. Rev. A* **73**, 013201 (2006).
- [54] A. Thuppilakkadan, J. Jose, and H. R. Varma, Systematic study of Coulomb confinement resonances of atoms trapped inside charged fullerenes, *Phys. Rev. A* **102**, 062826 (2020).
- [55] A. Thuppilakkadan, J. Jose, and H. R. Varma, Confinement enhanced spin-orbit interchannel coupling effect on the atomic photoionization, *J. Phys. B: At., Mol. Opt. Phys.* **54**, 145001 (2021).
- [56] V. K. Dolmatov, G. T. Craven, E. Guler, and D. Keating, Revivification of confinement resonances in the photoionization of Ar@C $60$  endohedral atoms far above thresholds, *Phys. Rev. A* **80**, 035401 (2009).
- [57] C. Brink, P. Hvelplund, H. Shen, H. A. Jiménez-Vázquez, R. J. Cross, and M. Saunders, Collisional fragmentation of Ar@C $60$ , *Chem. Phys. Lett.* **286**, 28 (1998).
- [58] M. Saunders, R. J. Cross, H. A. Jiménez-Vázquez, R. Shimshi, and A. Khong, Noble gas atoms inside fullerenes, *Science* **271**, 1693 (1996).
- [59] H. R. Varma, P. C. Deshmukh, V. K. Dolmatov, and S. T. Manson, Correlation and relativistic effects on the photoionization of confined atoms, *Phys. Rev. A* **76**, 012711 (2007).
- [60] V. K. Dolmatov, P. Brewer, and S. T. Manson, Photoionization of atoms confined in giant single-walled and multiwalled fullerenes, *Phys. Rev. A* **78**, 013415 (2008).
- [61] P. C. Deshmukh, A. Mandal, S. Saha, A. S. Kheifets, V. K. Dolmatov, and S. T. Manson, Attosecond time delay in the photoionization of endohedral atoms Ar@C $60$ : A probe of confinement resonances, *Phys. Rev. A* **89**, 053424 (2014).
- [62] J. George, H. R. Varma, P. C. Deshmukh, and S. T. Manson, Photoionization of atomic krypton confined in the fullerene C $60$ , *J. Phys. B: At., Mol. Opt. Phys.* **45**, 185001 (2012).
- [63] A. Thuppilakkadan, J. Jose, and H. R. Varma, Photoionization dynamics of Ar trapped in a fullerene anion: Coulomb confinement resonances in  $2s$  subshell and its impact on the  $3s$  subshell, *Phys. Scr.* **96**, 104004 (2021).
- [64] A. Kumar, H. R. Varma, P. C. Deshmukh, S. T. Manson, V. K. Dolmatov, and A. Kheifets, Wigner photoemission time delay from endohedral anions, *Phys. Rev. A* **94**, 043401 (2016).
- [65] W. R. Johnson and C. D. Lin, Multichannel relativistic random-phase approximation for the photoionization of atoms, *Phys. Rev. A* **20**, 964 (1979).
- [66] W. R. Johnson, C. D. Lin, K. T. Cheng, and C. M. Lee, Relativistic random-phase approximation, *Phys. Scr.* **21**, 409 (1980).
- [67] W. R. Johnson and K. T. Cheng, Photoionization of the outer shells of neon, argon, krypton, and xenon using the relativistic random-phase approximation, *Phys. Rev. A* **20**, 978 (1979).
- [68] I. Jordan, M. Huppert, S. Pabst, A. S. Kheifets, D. Baykusheva, and H. J. Wörner, Spin-orbit delays in photoemission, *Phys. Rev. A* **95**, 013404 (2017).
- [69] P. Ge, Y. Fang, Z. Guo, X. Ma, X. Yu, M. Han, C. Wu, Q. Gong, and Y. Liu, Probing the Spin-Orbit Time Delay of Multiphoton Ionization of Kr by Bicircular Fields, *Phys. Rev. Lett.* **126**, 223001 (2021).
- [70] J. Wragg, D. D. A. Clarke, G. S. J. Armstrong, A. C. Brown, C. P. Ballance, and H. W. van der Hart, Resolving Ultrafast Spin-Orbit Dynamics in Heavy Many-Electron Atoms, *Phys. Rev. Lett.* **123**, 163001 (2019).

- [71] U. Heinzmann and J. H. Dil, Spin-orbit-induced photoelectron spin polarization in angle-resolved photoemission from both atomic and condensed matter targets, *J. Phys.: Condens. Matter* **24**, 173001 (2012).
- [72] M. Y. Amusia, L. V. Chernysheva, and V. K. Dolmatov, Confinement and correlation effects in the Xe@C<sub>60</sub> generalized oscillator strengths, *Phys. Rev. A* **84**, 063201 (2011).
- [73] V. K. Dolmatov and D. A. Keating, Xe 4*d* photoionization in Xe@C<sub>60</sub>, Xe@C<sub>240</sub>, and Xe@C<sub>60</sub>@C<sub>240</sub>, *J. Phys.: Conf. Ser.* **388**, 022097 (2012).
- [74] M. H. Javani, H. S. Chakraborty, and S. T. Manson, Valence photoionization of noble-gas atoms confined in the fullerene C<sub>60</sub>, *Phys. Rev. A* **89**, 053402 (2014).
- [75] E. M. Nascimento, F. V. Prudente, M. N. Guimarães, and A. M. Maniero, A study of the electron structure of endohedrally confined atoms using a model potential, *J. Phys. B: At., Mol. Opt. Phys.* **44**, 015003 (2010).
- [76] S. Saha, A. Thuppilakkadan, H. R. Varma, and J. Jose, Photoionization dynamics of endohedrally confined atomic H and Ar: A contrasting study between compact versus diffused model potential, *J. Phys. B: At., Mol. Opt. Phys.* **52**, 145001 (2019).
- [77] C. Winstead and V. McKoy, Elastic electron scattering by fullerene, C<sub>60</sub>, *Phys. Rev. A* **73**, 012711 (2006).
- [78] M. E. Madjet, T. Renger, D. E. Hopper, M. A. McCune, H. S. Chakraborty, J.-M. Rost, and S. T. Manson, Photoionization of Xe inside C<sub>60</sub>: Atom-fullerene hybridization, giant cross-section enhancement, and correlation confinement resonances, *Phys. Rev. A* **81**, 013202 (2010).
- [79] E. Lindroth and J. M. Dahlström, Attosecond delays in laser-assisted photodetachment from closed-shell negative ions, *Phys. Rev. A* **96**, 013420 (2017).
- [80] E. V. Gromov, S. Klaiman, and L. S. Cederbaum, How many bound valence states does the C<sub>60</sub><sup>-</sup> anion have? *Phys. Chem. Chem. Phys.* **18**, 10840 (2016).